

See discussions, stats, and author profiles for this publication at: <https://www.researchgate.net/publication/233736695>

# Reduced Workfunction Intermetallic Seed Layers Allow Growth of Porous n-GaN and Low Resistivity, Ohmic Electron Transport

ARTICLE in ACS APPLIED MATERIALS & INTERFACES · NOVEMBER 2012

Impact Factor: 6.72 · DOI: 10.1021/am3020668 · Source: PubMed

---

CITATIONS

8

READS

74

## 7 AUTHORS, INCLUDING:



Oleksandr Bilousov

Universitat Rovira i Virgili

10 PUBLICATIONS 24 CITATIONS

[SEE PROFILE](#)



Joan J Carvajal

Universitat Rovira i Virgili

155 PUBLICATIONS 959 CITATIONS

[SEE PROFILE](#)



Xavier Mateos

Universitat Rovira i Virgili

219 PUBLICATIONS 2,190 CITATIONS

[SEE PROFILE](#)



Colm O'Dwyer

University College Cork

166 PUBLICATIONS 1,515 CITATIONS

[SEE PROFILE](#)

# Reduced Workfunction Intermetallic Seed Layers Allow Growth of Porous *n*-GaN and Low Resistivity, Ohmic Electron Transport

Oleksandr V. Bilousov,<sup>†</sup> Joan J. Carvajal,<sup>\*,†</sup> Dominique Drouin,<sup>‡</sup> Xavier Mateos,<sup>†</sup> Francesc Díaz,<sup>†</sup> Magdalena. Aguiló,<sup>†</sup> and Colm O'Dwyer<sup>\*,§,||,⊥</sup>

<sup>†</sup>Física i Cristallografia de Materials i Nanomaterials (FiCMA-FiCNA) and EMaS, Universitat Rovira i Virgili (URV), Marçalí Domingo s/n, E-43007 Spain

<sup>‡</sup>Department of Electrical and Computer Engineering, Université de Sherbrooke, Sherbrooke, PQ, J1K 2R1, Canada

<sup>§</sup>Applied Nanoscience Group, Department of Chemistry, University College Cork, Cork, Ireland

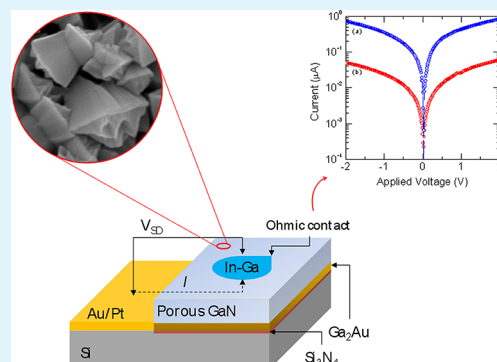
<sup>||</sup>Materials and Surface Science Institute, University of Limerick, Limerick, Ireland

<sup>⊥</sup>Micro & Nanoelectronics Centre, Tyndall National Institute, Dyke Parade, Cork, Ireland

## Supporting Information

**ABSTRACT:** Porous GaN crystals have been successfully grown and electrically contacted simultaneously on Pt- and Au-coated silicon substrates as porous crystals and as porous layers. By the direct reaction of metallic Ga and NH<sub>3</sub> gas through chemical vapor deposition, intermetallic metal-Ga alloys form at the GaN–metal interface, allowing vapor–solid–solid seeding and subsequent growth of porous GaN. Current–voltage and capacitance–voltage measurements confirm that the intermetallic seed layers prevent interface oxidation and give a high-quality reduced workfunction contact that allows exceptionally low contact resistivities. Additionally, the simultaneous formation of a lower workfunction intermetallic permits ohmic electron transport to n-type GaN grown using high workfunction metals that best catalyze the formation of porous GaN layers and may be employed to seed and ohmically contact a range of III–N compounds and alloys for broadband absorption and emission.

**KEYWORDS:** porous GaN, ohmic electron transport



## 1. INTRODUCTION

GaN and its related alloys such as InN and AlN that span the UV–vis–NIR spectrum have received much attention in the realization of new devices for electronics, microwave, and optoelectronics/photonics applications. With large bandgap energies, high breakdown fields, large carrier velocities, and a tolerance to high junction temperatures, the nitrides have a myriad of possibilities, including LEDs,<sup>1</sup> lasers for reading or storing data on high density optical media, solar blind detectors, biological monitoring, gas sensing,<sup>2</sup> and high temperature/high power electronics.<sup>3</sup>

The discovery of light-emitting nanoporous Si<sup>4</sup> propelled investigations of porosity formation in III–V and Group IV semiconductors.<sup>5–7</sup> Their unique properties compared to their bulk counterparts<sup>8</sup> have advanced their use in sensors, interfacial structures, and biomedical and catalysis applications.<sup>9–11</sup> Generally, pore formation in semiconductors can be obtained by anodizing them in a suitable electrolyte, under proper conditions;<sup>12</sup> however, the ability to form relatively uniform, crystalline porous GaN layers over large areas through complex etching without photolithographic masking or processing is challenging. For GaN, both wet and dry etching techniques have been unsuccessful in forming unique structures

of the material, and these methods can infer unwanted interface states and surface contamination that can affect transport properties by rendering the GaN surface more resistive. The double issue of dry etching techniques increasing GaN resistivity and wet etching techniques not as crystallographically controllable for GaN as it is for other III–V semiconductors, for example, can be alleviated by other growth methods involving seeding processes, some of which, as will be shown here, allow crystallographically delineated porous layers with improved contact resistivities.

Until now, nanoporous GaN thin films have received particular interest as buffer layers or templates for heteroepitaxial growth of lattice-mismatched materials with low defect density.<sup>13–15</sup> The porous material decreases the number of defects in the epitaxial layer, even when the lattice mismatch between the substrate and the GaN epitaxial layer is large, and it furthermore allows the growth of stress-realized epitaxies.<sup>1</sup> Extensions to wider and narrow gap InN and AlN, respectively, would allow the possibility of operation from the UV to IR

Received: September 21, 2012

Accepted: November 20, 2012

Published: November 20, 2012



wavelengths, and these materials are beginning to be investigated on the nanoscale.<sup>16–18</sup>

Porous GaN has been typically fabricated by (photo)-electrochemical and chemical etching methods,<sup>19–22</sup> giving textured surfaces as a result of pore coalescence and variations in etch rates for extended etching times. Metal catalysts are also used to initiate growth through either a vapor–liquid–solid (VLS)<sup>23,24</sup> or vapor–solid–solid (VSS)<sup>25,26</sup> mechanism when using molecular beam epitaxy (MBE) and chemical vapor deposition (CVD), where the catalyst can influence the growth; e.g., colloidal gold nanoparticles can initiate the growth of GaN nanowires. Additionally, as the ohmic contact technology to many III-N compounds is now well established<sup>27</sup> the marriage of seeded growth methods that infer alternative transport properties is an approach that could allow for new contacts to ternary and quaternary III-nitrides. Alternative techniques that allow band structure modification while also facilitating the direct growth of GaN, AlN, or InN, for example, with resulting low resistivity, ohmic contacts are thus of significant fundamental and commercial interest.

We produced porous GaN through the direct reaction of metallic Ga with NH<sub>3</sub> in a simple chemical vapor deposition (CVD) system.<sup>28</sup> Micrometer sized nanoporous GaN particles were grown directly onto boron nitride (BN) and silicon<sup>29</sup> substrates using this technique without necessitating any secondary electrochemical or electroless etching or subsequent chemical treatment after growth to induce porosity. Furthermore, it is possible to deposit porous GaN directly onto Si substrates in a single growth step. The development of porous GaN augers well for new electronic and optoelectronic devices with improved external quantum efficiencies, the incorporation of phosphors for LEDs, and high surface area sensing.<sup>30,31</sup>

Here, we report the successful growth and simultaneous electrical contacting of nanoporous GaN grown using high workfunction Au- and Pt-coated silicon substrates, through the direct reaction of Ga and NH<sub>3</sub> in the CVD system. Au and Pt both acted as a catalyst for the synthesis of porous GaN and result in the formation of an intermetallic compound at the GaN–metal interface that prevents oxidation of the GaN, promotes vapor–solid–solid growth of porous, single crystals, and in parallel allows for high-quality ohmic electrical contacts to the porous layers facilitated by a significantly reduced Schottky barrier height.

## 2. EXPERIMENTAL SECTION

**2.1. Synthesis of GaN Particles.** Nanoporous GaN microparticles were deposited using a Chemical Vapor Deposition (CVD) system on Au- and Pt-coated silicon (100) substrates with an area of 1 cm<sup>2</sup>, using a horizontal single-zone split tubular furnace Thermolyne 79300. Figure S1, Supporting Information, shows a schematic of the experimental setup. The system consists of a quartz tube inside of which a BN support is placed that holds the Si substrates during the growth experiments. The BN support has a hole in its center that allows exposure of the Si substrate to the Ga source. Gallium metal (99.99%) and ammonia (>99.98%) were used as the Ga and N sources, respectively. An excess amount of Ga was placed at the bottom of the quartz tube, in close contact with the temperature-controlling thermocouple. A 20 nm layer of Au or Pt was deposited on Si substrates using an RF sputtering process (AJA International) at a power of 150 W and a pressure of 3 mTorr. The coated substrate was placed 2 cm above the Ga source as can be seen in the schematic of the experimental setup shown in Figure S1 (Supporting Information). The quartz tube of the furnace was degassed to a vacuum pressure of 1 × 10<sup>-2</sup> Torr, after which NH<sub>3</sub> was introduced through a mass-flow controller at a flow rate of 75 sccm and the furnace heated to the

reaction temperature of 1203 K at a rate of 100 K min<sup>-1</sup>, while the pressure was kept at 15 Torr. The reaction was continued at this temperature and pressure for 60 min under a constant flow of NH<sub>3</sub>. Growth was halted by cooling to room temperature without NH<sub>3</sub> flow, reducing the pressure to 1 × 10<sup>-2</sup> Torr.

**2.2. Characterization.** The nanoporous GaN microparticles deposited on the Si substrates as a porous layer were characterized morphologically using a JEOL JSM 6400 scanning electron microscope (SEM). Before observation, samples were coated with a thin layer of gold with a Bal-Tec SCD004 sputterer.

Pore shapes, lengths, and propagation directions were analyzed by focused ion beam (FIB)-based tomography, i.e., time-resolved serial slicing and imaging with a Zeiss 1540 Cross Beam microscope (see Supporting Information). This dual beam system is equipped with a FIB column with a Ga source and a high-resolution field emission electron column. The FIB column stands at 52° to the electron column, and the sample surface is perpendicular to the ion column. The ion milling was performed using a 5 pA beam current to minimize surface damage and material redeposition.

X-ray diffraction (XRD) spectra and imaging in θ–2θ geometry of the as-grown sample were made using Cu Kα radiation in a Bruker-AXS D8-Discover diffractometer equipped with parallel incident beam (Göbel mirror), vertical θ–θ goniometer, XYZ motorized stage, and a General Area Diffraction Detection System (GADDS) HI-STAR detector with a multiwire proportional counter of 30 × 30 cm<sup>2</sup> area and 1024 × 1024 pixel density. Samples were placed directly on the sample holder, and the area of interest was selected with the aid of a video-laser focusing system. An X-ray collimator system allows the analysis of 500 μm<sup>2</sup> surface areas. The X-ray diffractometer was operated at 40 kV and 40 mA to generate Cu Kα radiation. We collected 2D XRD patterns covering a range of 2θ between 20 and 85° at a distance of 15 cm from the sample. The exposure time was 120 s per frame. Identification of the crystalline phases was achieved by comparison of the XRD diffractogram with the ICDD database using Diffrac<sup>plus</sup> Evaluation software (Bruker 2007).

High-resolution transmission electron microscopy (HRTEM) and convergent beam electron diffraction (CBED) were conducted on a JEOL 2100F FEGTEM operating at 200 kV and on a JEOL FEM 3000F TEM. Lattice resolution energy-dispersive X-ray analysis (EDAX) was acquired using the EDX Genesis XM 4 system 60 detector.

Charge transport measurements through the porous GaN films were conducted using two- and four-probe measurements using a dc-voltage and an Agilent 34401A Digital Multimeter in a Peltier cell, thermostatted to 295 K in a Faraday cage. Liquid metal contacts were made using In–Ga eutectic blown into a sphere from a gold metallized short borosilicate capillary tube, ensuring good wetting (several μm<sup>2</sup>) to the rough top-surface morphology of the porous GaN and avoiding electrical shorting to the underlying metallized silicon. Measurements were made in two-probe, four-probe, and van der Pauw<sup>32</sup> geometry. Resistivity values were extracted from *I*–*V* curves in the high bias regime (series resistance) and also from four-point probe measurements. Capacitance–voltage analysis using gold Schottky contacts to porous GaN was performed by scanning the applied potential at a rate of 10 mV s<sup>-1</sup> with a superimposed AC signal with an amplitude of 15 mV at a frequency of 1 MHz.

## 3. RESULTS AND DISCUSSION

**3.1. Morphological Characterization of Porous GaN.** The resulting nanoporous GaN structures, deposited on the surfaces of Si substrates coated with Au and Pt, were characterized morphologically by SEM. Figures 1(a) and (b) show the typical porous GaN layer morphologies grown using this approach, and in Figures 1(c) and (d) we observe that the porous GaN particles have a characteristic morphology consisting of faceted hourglass crystals with a mean size of ~1.5 μm end-to-end. The GaN crystals have smooth lateral faces, while pores are observed on their basal planes, similar to

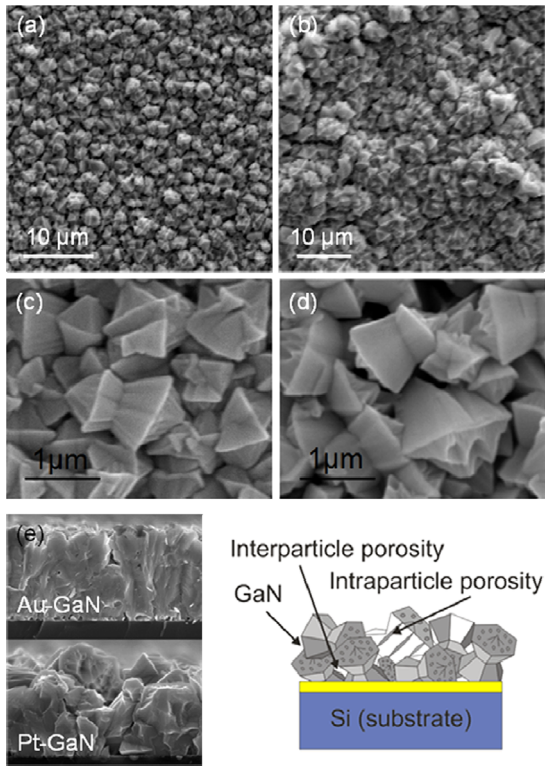


**Figure 1.** SEM images of porous GaN particles grown on Si(100) substrates coated with (a,c) 20 nm film of Au and (b,d) 20 nm film of Pt. (e) Cross-sectional SEM images of the GaN layers for each system (bottom left) and schematic representation of a sample of GaN nanoporous particles grown on a Si substrate coated with Au showing the interparticle and intraparticle porosity of the GaN layers (bottom right).

those we observed on BN substrates<sup>28</sup> or Si substrates coated with  $\text{Ni}(\text{NO}_3)_2$ .<sup>29</sup> Crystal growth occurs progressively on the surface with individual crystals ripening until a layer of porous GaN microparticles covers the surface as a porous layer. The particles obtained on the Si substrates coated with Pt showed a higher degree of internal porosity, with the pores aligned along the [0001] direction, than those grown from Au-coated Si substrates. Figure S2 (Supporting Information) shows the energy dispersive X-ray (EDX) spectra for these two samples, showing the contents of Ga and N in these porous particles. The concentration of N is lower than expected due to the low atomic weight of this atom, which is difficult to detect by using this technique.

The GaN layers are both microporous and mesoporous. The microporosity stems from the free space between particles (see Figures 1(c) and (d)), whereas the nanoscale mesoporosity comes from internal pore features within the particles, confirmed with time-resolved FIB-based tomography, shown in Figure 2(a,b,c) together with the simulation of the external morphology of the particle, shown in Figure 2(d). With this technique, we analyzed the shape and length of the pores, as well as their direction of propagation inside of the GaN particles by removing the material, slice-by-slice, using ion-milling, closer to the lateral surfaces of the GaN nanoporous particle. The secondary electron images recorded concurrently revealed straight pores with lengths similar to the dimension of the GaN particles. These pores are parallel to the facet direction and do not intersect nor branch, as can be seen in the video milling sequence in the Supporting Information. In some cases,

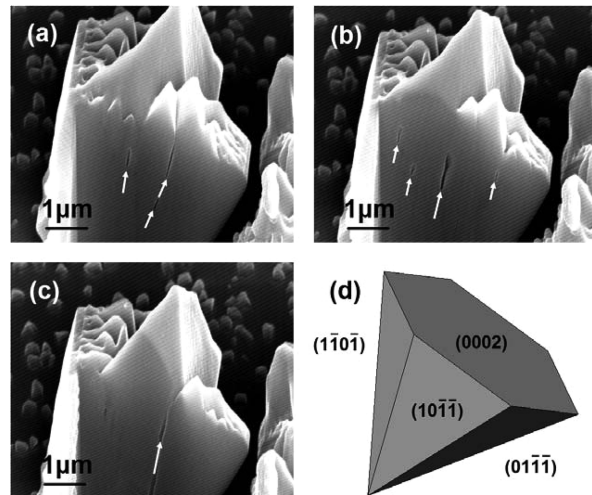


**Figure 2.** FIB tomography acquired with a milling current of 5 pA for a duration of 160 s revealing the GaN intraparticle porosity (a,b,c) and simulation of the morphology of the GaN crystal with terminating crystal planes identified (d).

the initiation of epitaxial polycrystalline segments within an hourglass crystal is also found as shown in Figure 2c. The diameters of the pores ranged from 50 to 100 nm, with negligible variation in diameter with length (nontapered). From these images and the video recorded during the tomography (see Supporting Information) performed on different GaN particles, we conclude that the nanopores in the central part of the GaN particles follow an orientation parallel to the [0001] crystallographic direction. However, the nanopores found in the outer portions of the GaN particles are parallel to the lateral faces of these particles.

### 3.2. Structural Characterization of VSS Porous GaN.

The crystalline structure of the porous GaN particles deposited on Si substrates coated with Au and Pt was analyzed using X-ray diffraction. The XRD pattern shown in Figure 3(b) for GaN grown on Au-coated Si substrates confirms crystalline wurtzite GaN growth with a predominant diffraction intensity from low-index crystal facets. The regions at which the (400) diffraction peak of Si appears at  $69.131^\circ 2\theta$  have been excluded from the measurement to avoid intensity saturation. This allows observation of lower intensity reflections that are attributed to crystalline  $\text{Si}_3\text{N}_4$  and a crystalline Au–Ga intermetallic alloy of cubic  $\text{Ga}_2\text{Au}$ . We believe that the  $\text{Si}_3\text{N}_4$  formation is most likely due to reaction between  $\text{NH}_3$  and silicon accelerated by the metallic catalyst.

The formation of the Au–Ga crystalline alloy, which occurs here above the solid-solution formation temperature of 923 K, confirms intermetallic seeding to form GaN by reaction with  $\text{NH}_3$  through a vapor–solid–solid process. The uniform intensity of the Debye rings (along the curved ring portions in Figure 3(c)) collected for porous GaN confirms that there is no texturing in the layer of porous crystals (see Figure 3(c)).

HRTEM measurements were carried out to confirm the crystallinity of the nanoporous GaN crystals. Figure 3(d) shows low- and high-magnification HRTEM images of a typical porous GaN particle. Pores are not directly observable here due to the thickness of the crystal. In the high-magnification image, the two-dimensional atomic structure of the GaN crystal is resolved. In this figure we identified two different  $d$ -spacings of 0.52 and 0.28 nm corresponding to the (0001) and (10–10)

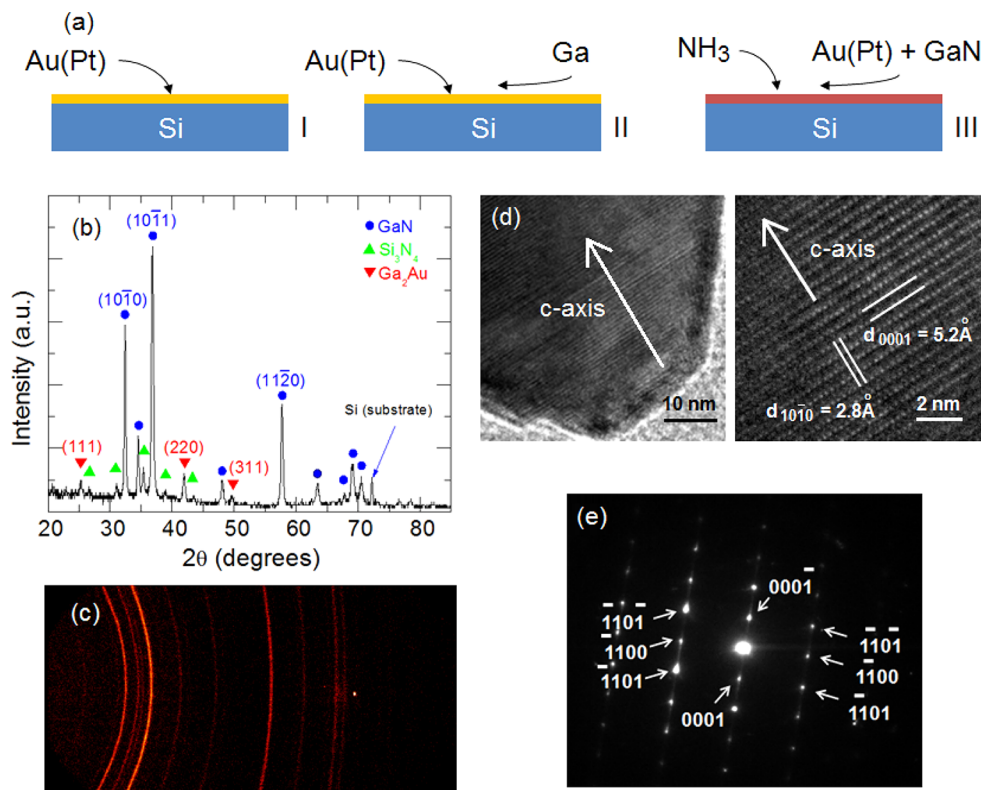


**Figure 3.** (a) Mechanism of growth of the GaN nanoporous particles through the VSS process. (b) XRD pattern for porous GaN deposited on Au-coated Si(100) showing the formation of crystalline GaN (ICDD 01-073-7289), Si<sub>3</sub>N<sub>4</sub> (ICDD 03-065-8613), and Ga<sub>2</sub>Au alloy (ICDD 01-071-6479). (c) Debye rings recorded with a GADDS detector indicating no texturation of the porous GaN layer. (d) HRTEM image shows the presence of a few stacking faults and the two-dimensional atomic structure with *d*-spacings for the (0001) and (10-10) planes. (e) SAED zone [11-20] axis pattern.

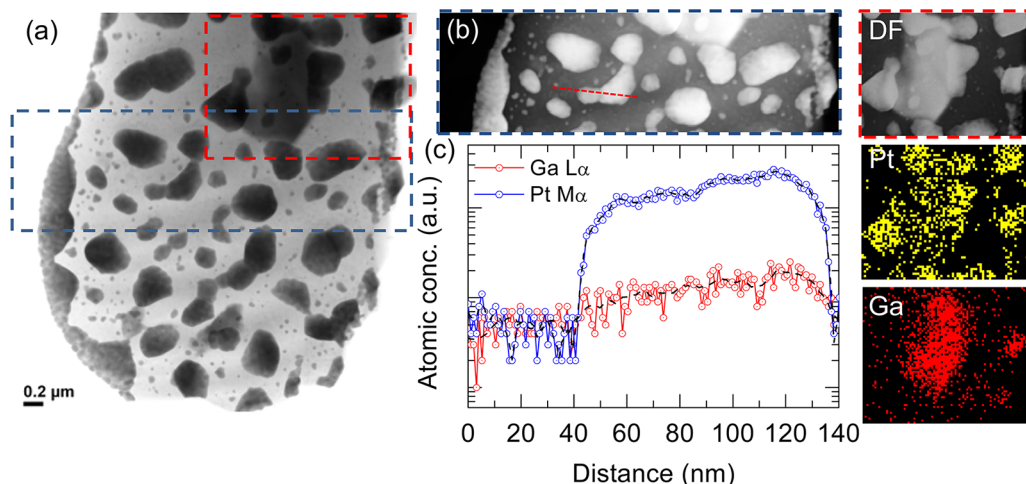


**Figure 4.** (a) Bright-field TEM image of the Pt–GaN intermetallic islands formed at the GaN interface and (b) corresponding dark-field STEM image with (c) corresponding line profiles of atomic concentration for the Ga L $\alpha$  and Pt M $\alpha$  X-rays. (Right) EDX maps confirming the presence of Pt and Ga in most metallic islands on the silicon surface.

planes of the GaN structure. Figure 3(e) shows a selected area electron diffraction (SAED) pattern taken from one of the corners of the GaN porous particle. This diffraction pattern corresponds to the wurtzite structure of GaN, confirming that the nanoporous GaN particle is a single crystal. The existence of some (0001) diffraction streaks that generated a splitting of the diffraction intensity in the SAED patterns suggests the existence of thin lamellar defects lying parallel to the (0001) plane;<sup>28</sup> stacking faults along the crystallographic *c*-axis can be

seen in the HRTEM image in Figure 3(d). The growth of these GaN nanoporous particles is assisted by a solid particle through the vapor–solid–solid (VSS) mechanism, the main stages of which are: the Ga incorporation into the Au or Pt solid phase eutectic, the formation of a Ga–Au or Ga–Pt alloy, the solubilization of nitrogen in the Ga–Au(Pt) alloy, and finally the nucleation and growth of GaN (see Figure 3(a)).

For Pt-seeded VSS grown porous GaN, we examined the surface of the silicon substrate directly underneath the GaN

crystals. Figure 4(a) shows a bright-field TEM image of a portion of the silicon substrate where the Pt–GaN seed crystals (dark regions) are found. The seeds have characteristic faceted morphology and shape, and the deposit comprises fused grains. EDX analysis in Figure 4(b) confirms the presence of both Pt and Ga, and while the intensity of Pt is greater as would be expected, the atomic concentration of Ga follows that of Pt, where the variation stems from increasing seed crystal volume along the line scan. Corresponding mapping of the intermetallic Pt–GaN seeds in Figure 4 confirms that not all of the Pt particles contain Ga, i.e., that a proportion of the metallic seeds take up Ga to form the intermetallic, but it should be noted that the site of interest examined is taken from a region of the substrate between fully grown GaN crystals. As with the Ga<sub>2</sub>Au seeds, the Pt–GaN seeds are where VSS GaN growth starts, but a crystalline diffraction pattern is not found for this phase as readily as for Au-seeded GaN.

**3.3. Electrical Characterization of Pt- and Au-Contacted Porous GaN.** An important consideration for porous layers is that electrically they are sensitive to grain boundary density, and when rough, the sheet and contact resistances ( $\rho_c$ ) are influenced not only by the physical state of the interface at the contact but also by the geometry. In all cases, the ability to accurately evaluate the contacts is critical. The standard techniques of linear transmission line measurements (TLMs) and circular TLM (c-TLM) have been established.<sup>12</sup> For porous GaN specifically, the thickness is determined by the size of the crystals and their assembly on the surface, which results in a “rough” topology, with a high density of grain boundary scattering centers. For thin GaN layers with higher (than thick smooth epi-layers) sheet resistance ( $R_s$ ), the accuracy of the TLM-type approaches becomes an issue. Here, although the layers are quite thick compared to epi-layers of GaN on LED structures for example, their  $R_s$  values are expected to be close to that of thin epi-layers. Thus, both TLM and less geometrically sensitive van der Pauw measurements were acquired to probe the transport mechanism but also the contact resistivity and its contribution to the overall resistance, a contribution that decreases with improving  $\rho_c$ .

Figure 5 shows the  $I$ – $V$  curves from the porous GaN catalyzed by Pt (Figure 5(a)) and also by Au (Figure 5(b)), with the second contact placed on the underlying metal, as shown schematically in Figure 5. The  $\ln(I)$ – $V$  curves show only slight asymmetry indicative of near-ohmic, weak Schottky barriers to Pt and Au. Consistently, the conductivity of porous GaN grown from Pt is higher than that grown from Au. In such cases, there is no detectable presence of any remaining Ga–Pt phases between the catalyzed GaN and the contact metal. The  $I$ – $V$  curve of porous GaN–Pt in Figure 5c shows the low-bias nonlinearity consistent with such a weak Schottky barrier. Both contacts fit with thermionic emission theory, acknowledging a near potential-independent high ideality factor for near-ohmic barriers. In any diode, a number of transport mechanisms play a role, including diffusion and tunneling currents in addition to thermionic emission. At room temperature, the effective linearity of the  $I$ – $V$  response measured for porous GaN to high work function metals, with an intermetallic seed layer between the metal and GaN, is maintained at high bias. Since the ideality factor does not change due to near-ohmic response, the differential resistance and series resistance values are quite similar, as will be shown below. The Schottky barrier height (SBH) can still be estimated from

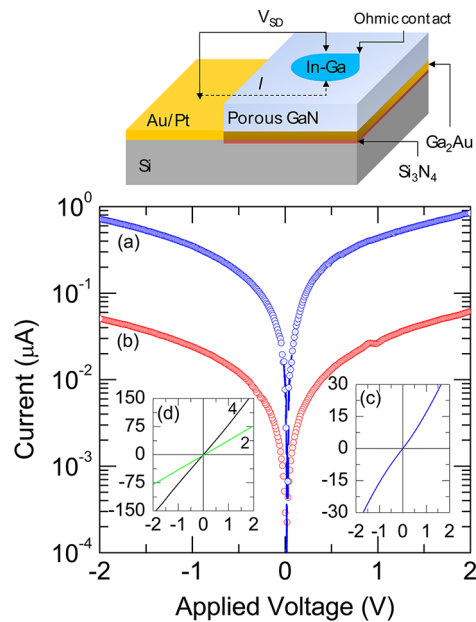


**Figure 5.** (Top) Schematic representation of the contacted porous GaN layer. (Bottom)  $\ln(I)$ – $V$  curves for porous GaN grown from (a) Pt and (b) Au. (c)  $I$ – $V$  curve for the porous GaN grown directly from Pt and (d)  $I$ – $V$  curves from two- and four-probe measurements using In–Ga ohmic contacts to porous GaN.

$$I = I_0 \left[ \exp\left(\frac{qV - IR_S}{kT}\right) - 1 \right] \quad (1)$$

where  $I_0 = AA^{**}T^2 \exp(-q\varphi_{B,n}^0/kT)^{33}$  where  $A^{**}$  is the effective Richardson constant. The estimated SBHs using the theoretical value for the effective Richardson constant (26.4 A cm<sup>-2</sup> K<sup>-2</sup>) for Pt and Au contacted porous GaN are 0.66 and 0.53 eV, respectively.

Effective ohmic contacts can form with n-type GaN suggesting that the grain boundary scattering or resistivity dominates transport through an alloyed interface that promotes ohmic transport in a far from ideal diode arrangement where current flow is through the contact. Two terminal transport measurements (Figure 5d) acquired between the In–Ga ohmic contacts showed perfect ohmicity. Corresponding four-probe analysis gives sheet resistances for porous GaN films in the range 4.3–4.9 kΩ/◻. The van der Pauw measurements confirm these values independent of contact area and effective geometry on rough surfaces. Additionally, it is important to note that deposited Pt (and Au) forms coarsened NP distributions after the growth of GaN, due primarily to temperature-mediated coalescence and ripening. For electrical measurements, particle distributions confirm that both nearest-neighbor distances and overall distribution of various non-spherical particles prevent the formation of a percolating conduction layer beneath the GaN; the electrical characterization is of the porous GaN polycrystalline layer.

Contact resistivities were determined with variable inter-contact separation using the transmission line measurement (TLM) approach. For the contact resistivity of the rough, faceted top surface, we assume that the semiconductor sheet resistance underneath the contacts remains unchanged. This is reasonable since no alloyed contacts (referring to the drain contact, not the interfacial metal–GaN layer) are used which is known to affect sheet resistance.<sup>34</sup> In spite of higher porosity from Pt-grown porous GaN, low contact resistivities between

$2.2\text{--}4.1 \times 10^{-4} \Omega \text{ cm}^2$  for Pt-catalyzed *n*-GaN and  $5.9\text{--}8.8 \times 10^{-4} \Omega \text{ cm}^2$  from Au-mediated porous *n*-GaN layers are found. Current flow from the porous GaN to the metal is assumed to flow horizontally through the intermetallic seed layer at the GaN interface and collected at the Au or Pt metallized silicon. Leakage currents from the slightly more resistive intermetallic seed layers are prevented by the formation of a crystalline dielectric  $\text{Si}_3\text{N}_4$  layer. This approach is valid as long as the injection of current across the contact is uniform. The current spreading length, which is a measure of the effective length over which current is injected into the porous GaN layer, is given by  $L_S = \sqrt{(\rho_c/R_S)}$  and holds for epi-layer systems with two ohmic contacts. From a TLM measurement, we find that the contribution from the contacts to the overall series resistance between them scales with  $\sqrt{\rho_c}$  as would be expected from a double ohmic contact system, in spite of high workfunction metals contacting a rough, *n*-type GaN layer. The accuracy of  $\rho_c$  is limited by its relative value compared to the total intercontact resistance; lower  $\rho_c$  relates to smaller contributions and increased errors in its determination from TLM measurements and the geometry of wetting liquid metal contacts to a rough, faceted porous GaN layer, which is unavoidable. Definitive nonlinearity in the *I*–*V* response and also variations in site-to-site measurement can also contribute to these errors. Here, as the GaN is unintentionally *n*-type and consequently has a more uniform doping profile as a function of distance than corresponding *p*-type layers which require temperature-mediated activation, site-to-site variations were found to be minimal and varied by  $\sim 0.6\%$ .

Compared to the  $R_S$  values, it is clear that an effective ohmic contact is formed, and sheet and series resistances through the GaN layer are dominated by the layer structure. The overall series resistance,  $R$ , to which the sheet and contact resistivities contribute can also be determined from the thermionic emission theory described above. In the presence of the intermetallic contact, the transport is effective ohmic. The series resistance can also be obtained from the differential conductance through its proportionality to the current according to

$$\frac{dI}{dV} = \left( R_S + \frac{kT}{q} \left[ \frac{1/I_0}{I/I_0 - 1} \right] \right)^{-1} \quad (2)$$

For the thermionic emission-based transport through the porous *n*-GaN layer, the reciprocal of  $dI/dV$  approaches  $R_S$  at the higher currents, provided that the ideality factor remains unchanged, which is the case here. The differential resistance is plotted in Figure 6b. As observable from the *I*–*V* curves in Figure 6a, the response from Pt contact porous GaN is slightly less symmetric and thus has a slightly higher Schottky barrier, giving very weak rectification with a reverse bias current that is potential dependent. From Figure 6b, we find that the differential conductance curves confirm this variation in contact type, where porous GaN grown from a seed layer of  $\text{Ga}_2\text{Au}$  exhibits an essentially horizontal response indicative of a linear *I*–*V* curve; the slope varies for Pt-seeded contacts consistent with a slight nonlinearity in the *I*–*V* response and also a higher overall (by a factor of 10–13) conductance compared to Au-seeded porous *n*-GaN.

It is worth noting that the *n*-type contacts were effectively ohmic as deposited and did not need any postdeposition annealing to induce this effective ohmicity; such linear *I*–*V* behavior is not found with Au contacts, and the intermetallic

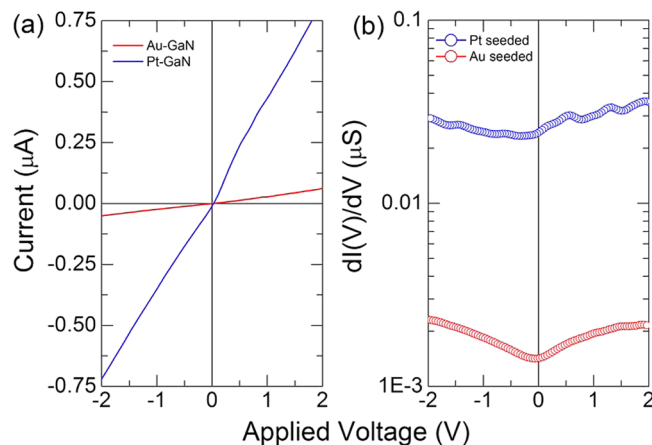


**Figure 6.** Room temperature (a) *I*–*V* and (b) differential conductance ( $dI(V)/dV$ ) for Au- and Pt-seeded porous GaN layers.

seed layer interface is critical for removing the transport Schottky barrier. The values match those of MBE grown GaN thin films with Ti/Au alloy contacts after annealing to 973 K<sup>35</sup> and are caused by the efficient interface between the metal and the growing porous GaN. Additionally, since annealing at 1173 K is known to initially improve contact resistivities down to  $10^{-6} \Omega \text{ cm}^2$  with ohmic Ti/Al contacts, continued heating at this temperature for more than 40 s has been shown to result in a drastic increase in  $\rho_c$ .<sup>35</sup> The present method avoids this by the use of noble metal contacts as catalysts and solid seed layers for the GaN growth and as electrodes for transport measurements.

Capacitance–voltage analysis was performed by scanning the applied potential at a rate of 10 mV s<sup>-1</sup> with a superimposed AC signal with an amplitude of 15 mV at a frequency of 1 MHz to determine the capacitance of the porous GaN under depletion conditions. For these porous GaN layers, this frequency was sufficient to sinusoidally vary the depletion region width without unwanted contributions to capacitance from the dielectric  $\text{Si}_3\text{N}_4$  present at the  $\text{Ga}_2\text{Au}$  interface. Gold contacts were made to the porous GaN and formed a Schottky contact for the measurement. The  $1/C^2$ –*V* analysis in the framework of the Mott–Schottky model, shown in Figure 7(a), confirms an unintentional *n*-type GaN with a donor concentration  $N_D$  given by the slope  $N_D = 2C^2V/q\epsilon\epsilon_0$  corresponding to a net impurity concentration<sup>36</sup> in porous GaN of  $n = 1.6 \times 10^{16} \text{ cm}^3$  using a dielectric constant  $\epsilon = 8.9$  for GaN. These low values for unintentionally doped *n*-GaN give a corresponding SBH from

$$\varphi_{B,n}^0 = eV_{bi} + eV_n + kT \quad (3)$$

where  $eV_{bi}$  is the barrier height from the voltage intercept and  $eV_n = E_{C,n} - E_F$ , of  $0.78 \pm 0.1 \text{ eV}$  and  $0.62 \pm 0.1 \text{ eV}$  for Pt-GaN and Au-GaN, respectively. Minima in differential capacitance indicating transition beyond depletion conditions are also found close to the respective values for the built-in potential of these Schottky junctions. These values are lower than standard epi-layer of *n*-GaN, even when accounting for image force lowering of the barrier height in this case. The Fermi level energy with respect to the Pt and Au workfunction is markedly reduced compared to standard values owing to the interfacial alloy<sup>37</sup> whose work function is less than the respective noble metal, giving lower Schottky barriers to carrier transport through the high grain-boundary density GaN layer. This is also reflected in the carrier mobilities, which for a doping density of

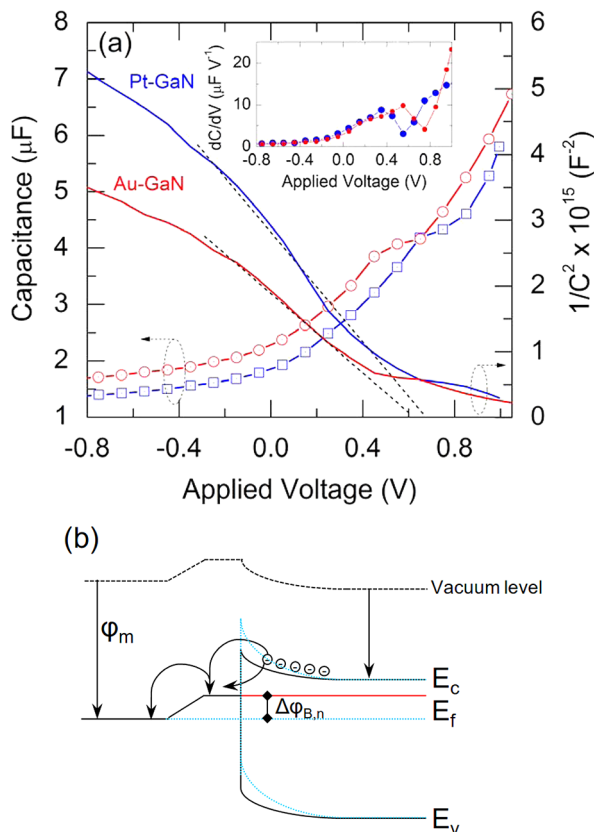


**Figure 7.** (a) Interface capacitance and Mott–Schottky ( $1/C^2 - V$ ) profile for Pt- and Au-catalyzed porous GaN layers. (b) Proposed band structure model for intermetallic interface phase formation acting as the effective ohmic contact. The barrier with (solid line) and without (dashed line) the presence of the intermetallic is shown.

effectively  $\sim 10^{16} \text{ cm}^{-3}$  an average electronic mobility of  $\sim 208 \text{ cm}^2 \text{ V}^{-1} \text{ s}^{-1}$  is determined.

A plausible band structure for the interfacial intermetallic contact is also shown in Figure 7(b), which shows the presence of the  $\text{Ga}_2\text{Au}$  interface, with its lower workfunction, between the Au and GaN (a similar situation can be drawn when using Pt rather than Au). With forward bias, electrons can easily overcome the significantly reduced barriers, by thermionic-field emission to inject into the Au or Pt from the intermetallic. When the bias becomes negative, holes can tunnel through the Au/intermetallic interface barrier and inject into the notch to recombine with electrons. The contact resistance is markedly reduced as it provides a recombination center for carriers giving a linear  $I-V$  response.

For the low resistance contacts to a porous GaN layer, either a low barrier Schottky contact forms with a graded band gap interface or a tunnel contact is formed. From XRD analysis, a crystalline  $\text{Si}_3\text{N}_4$  dielectric layer forms when deposition is performed on silicon, just prior to continued VSS porous GaN growth, and is not likely from N out-diffusion from the GaN. The GaN, too, is not expected to decompose at 1203 K in  $\text{NH}_3$ ,<sup>38</sup> but the Au and Pt melting points are close to this temperature. These metals solidify once the crystalline  $\text{Ga}_2\text{Au}$  solid phase is formed as the GaN interface. Oxide growth that would increase the resistivity of the contact is also prevented at this growth interface. To examine the reduction in effective barrier height, we considered the possibility of the influence of  $\text{Ga}_2\text{O}_3$  formation between the intermetallic and the GaN, as is

widely known for metal contacts to GaN. The reduction in  $\phi_{B,n}^0$  is thus correlated with the absence of an insulating oxide and is detailed in the Supporting Information. The variance in  $V_{fb}$  from the C–V measurements, as observed in many metal/GaN systems, suggests Fermi-level pinning is not prevalent, and thus we do not consider surface state-mediated conduction or gap states to play a major role in effective ohmicity.

On Pt and Au, however, we confirm an intermetallic  $\text{Ga}_2\text{Au}$  phase typical of a VSS growth process which suggests a band structure that promotes transport by lowering the Schottky barrier by acting as a low barrier, ohmic contact to the GaN, rather than forming a definitive tunnel contact which shows ohmicity over a small potential range. In such a case, negative differential resistance caused by carrier effective mass increases, and reduction in mobility is prevented. The intermetallic formation at the interface that allows the growth of the GaN effectively acts as an intermetallic ohmic contact at the semiconductor interface, and the method may be extended to growing nanoscale III-N materials and alloys using metals that are not typically employed for contacting, to give ohmic response.

#### 4. CONCLUSIONS

Porous GaN particles have been successfully grown as high surface area layers from Pt- and Au-coated silicon substrates by a vapor–solid–solid process. The particles form as a layer of single-crystal particles with interparticle and intraparticle porosity. Current–voltage and capacitance–voltage measurements show near-ohmic transport through low-doped, polycrystalline (as a layer), porous  $n$ -GaN without alloy contacts or low work function metals. Metal–Ga intermetallic alloy formation during vapor–solid–solid growth promotes thermionic emission-based low-resistance ohmic transport through the porous layer, and very low contact resistivities are possible to the faceted, rough  $n$ -GaN surface. The ability of contacting the GaN using such metals while at the same time facilitating the growth in a high surface area, crystalline porous network, including intraparticle pores, gives opportunities for superior diode-based optoelectronics and sensing and also metallic or colloidal quantum dot inclusions to tune broad-band light emission characteristics. The overall method of using intermetallic as ohmic contacts could also be applied to simultaneously grow and contact nanoscale III-N compounds for optoelectronic devices.

#### ASSOCIATED CONTENT

##### S Supporting Information

A document with further details on the crystal growth setup (Figure S1) and energy dispersive X-ray (EDX) spectra for GaN samples grown on Si(100) substrates and coated with Pt and Au catalysts (Figure S2) is provided. The document also includes a short discussion about the effect that an interfacial oxide between the intermetallic layer and porous GaN would have on the electrical performance of the samples. Finally, a video showing the results obtained in time-resolved FIB tomography of a single porous GaN particle is also included to illustrate the intraporosity of the samples. This material is available free of charge via the Internet at <http://pubs.acs.org>.

#### AUTHOR INFORMATION

##### Corresponding Author

\*E-mail: joanJosep.carvajal@urv.cat; c.odwyer@ucc.ie.

**Notes**

The authors declare no competing financial interest.

**ACKNOWLEDGMENTS**

This work was supported by the EU Framework 7 under Project No. FP7-SPA-2010-263044, the Spanish Government under Projects No. MAT2011-29255-C02-02, TEC2010-21574-C02-02, PI09/90527, and by Catalan Authority under Project No. 2009SGR235. This work was also supported by Science Foundation Ireland under contract No. 07/SK/B1232a and under the framework of the INSPIRE programme, funded by the Irish Government's Programme for Research in Third Level Institutions, Cycle 4, National Development Plan 2007–2013. The authors are also grateful to V. Mogili and D. Tanner for STEM imaging.

**REFERENCES**

- (1) Lin, C. F.; Chen, K. T.; Lin, C. M.; Yang, C. C. *IEEE Electron Device Lett.* **2009**, *30*, 1057–1059.
- (2) Ramizy, A.; Hassan, Z.; Omar, K. *Sens. Actuators, B* **2011**, *155*, 699–708.
- (3) Nakamura, S.; Pearton, S.; Fasol, G. In *The Blue Diode Laser. The Complete Story*; Springer: Berlin, 2000; p 7.
- (4) Lehmann, V.; Gösele, U. *Appl. Phys. Lett.* **1991**, *58*, 856–858.
- (5) Tiginyanu, I. M.; Ursaki, V. V.; Monaico, E.; Foca, E.; Foll, H. *Electrochem. Solid-State Lett.* **2007**, *10*, D127–D129.
- (6) O'Dwyer, C.; Buckley, D. N.; Sutton, D.; Serantoni, M.; Newcomb, S. B. *J. Electrochem. Soc.* **2007**, *154*, H78–H85.
- (7) Stevens-Kalceff, M. A.; Tiginyanu, I. M.; Langa, S.; Foll, H.; Hartnagel, H. L. *J. Appl. Phys.* **2001**, *89*, 2560–2565.
- (8) Bressets, P. M. M. C.; Knappen, J. W. J.; Meulenkamp, E. A.; Kelly, J. *J. Appl. Phys. Lett.* **1992**, *61*, 108–110.
- (9) Huang, Y.; Duan, X.; Cui, Y.; Lieber, C. M. *Nano Lett.* **2002**, *2*, 101–104.
- (10) Zhou, T.; Cheng, D.; Zheng, M.; Ma, L.; Shen, W. *Nanoscale Res. Lett.* **2011**, *6*, 276.
- (11) Huang, J.; Ding, K.; Wang, X.; Fu, X. *Langmuir* **2009**, *25* (14), 8313–8319.
- (12) O'Dwyer, C.; Buckley, D. N.; Sutton, D.; Newcomb, S. B. *J. Electrochem. Soc.* **2006**, *153*, G1039–G1046.
- (13) Ghosh, B. K.; Tanikawa, T.; Hashimoto, A.; Yamamoto, A.; Ito, Y. *J. Cryst. Growth* **2003**, *249*, 422–428.
- (14) Mynbaeva, M.; Totkov, A.; Kryzhanovski, A.; Kotousova, I.; Zubrilov, A. S.; Ratnikov, V. V.; Davidov, V. Y.; Kuznetsov, N. I.; Mynbaev, K.; Tsvetkov, D.; et al. *MRS Internet J. Nitride Semicond. Res.* **1999**, *4*, 14.
- (15) Qhalid Fareed, R. S.; Adivarahan, V.; Chen, C. Q.; Rai, S.; Kuokstis, E.; Yang, J. W.; Khan, M. A.; Caissie, J.; Molnar, R. J. *Appl. Phys. Lett.* **2004**, *84*, 696–698.
- (16) Cui, K.; Fathololoumi, S.; Kibria, M. G.; Botton, G. A.; Mi, Z. *Nanotechnology* **2012**, *23*, 085205.
- (17) Wang, D.; Pierre, A.; Kibria, M. G.; Cui, K.; Han, X.; Bevan, K. H.; Guo, H.; Paradis, S.; Hakima, A.-R.; Mi, Z. *Nano Lett.* **2011**, *11*, 2353–2357.
- (18) Chang, Y.-L.; Li, F.; Fatehi, A.; Mi, Z. *Nanotechnology* **2009**, *20*, 345203.
- (19) Mynbaeva, M.; Titkov, A.; Kryganskii, A.; Ratnikov, V.; Mynbaev, K.; Huhtinen, H.; Laiho, R.; Dmitriev, V. *Appl. Phys. Lett.* **2000**, *76*, 1113–1115.
- (20) Wang, Y. D.; Chua, S. J.; Sander, M. S.; Chen, P.; Tripathy, S.; Fonstad, C. G. *Appl. Phys. Lett.* **2004**, *85*, 816–818.
- (21) Bae, S. Y.; Seo, H. W.; Park, J.; Yang, H.; Kim, B. *Chem. Phys. Lett.* **2003**, *376*, 445–451.
- (22) Diaz, D. J.; Williamson, T. L.; Adesida, I.; Bohn, P. W.; Molnar, R. J. *J. Appl. Phys.* **2003**, *94*, 7526–7534.
- (23) Wagner, R. S.; Ellis, W. C. *Appl. Phys. Lett.* **1964**, *4*, 89–90.
- (24) Gottschalch, V.; Wagner, G.; Bauer, J.; Paetzelt, H.; Shirnow, M. *J. Cryst. Growth* **2008**, *310*, 5123–5128.
- (25) Persson, A. I.; Larsson, M. W.; Stenström, S.; Ohlsson, B. J.; Samuelson, L.; Wallenberg, L. R. *Nat. Mater.* **2004**, *3*, 677–681.
- (26) Hou, W.-C.; Chen, L.-Y.; Tang, W.-C.; Hong, F. C. N. *Cryst. Growth Des.* **2011**, *11*, 990–994.
- (27) Song, J. O.; Ha, J.-S.; Seong, T.-Y. *IEEE Trans. Electron Devices* **2010**, *57*, 42–59.
- (28) Carvajal, J. J.; Rojo, J. C. *Cryst. Growth Des.* **2009**, *9*, 320–326.
- (29) Carvajal, J. J.; Bilousov, O. V.; Drouin, D.; Aguiló, M.; Díaz, F.; Rojo, J. C. *Microsc. Microanal.* **2012**, *18*, 1–7.
- (30) Mei, Y.; Thurmer, D. J.; Deneke, C.; Kiravittaya, S.; Chen, Y.-F.; Dadgar, A.; Bertram, F.; Bastek, B.; Krost, A.; Christen, J.; et al. *ACS Nano* **2009**, *3*, 1663–1668.
- (31) Liang, Z.; Wildeson, I. H.; Colby, R.; Ewoldt, D. A.; Zhang, T.; Sands, T. D.; Stach, E. A.; Benes, B.; García, R. E. *Nano Lett.* **2011**, *11*, 4515–4519.
- (32) O'Dwyer, C.; Szachowicz, M.; Visimberga, G.; Lavayen, V.; Newcomb, S. B.; Sotomayor Torres, C. M. *Nat. Nanotechnol.* **2009**, *4*, 239–244.
- (33) Fan, Z.; Mohammad, S. N.; Kim, W.; Aktas, O.; Botchkarev, A. E.; Morkoç, H. *Appl. Phys. Lett.* **1996**, *68*, 1672–1674.
- (34) Tracy, K. M.; Hartlieb, P. J.; Einfeldt, S.; Davis, R. F.; Hurt, E. H.; Nemanich, R. J. *J. Appl. Phys.* **2003**, *94*, 3939–3948.
- (35) Lin, M. E.; Ma, Z.; Huang, F. Y.; Fan, Z. F.; Allen, L. H.; Morkoç, H. *Appl. Phys. Lett.* **1994**, *64*, 1003–1005.
- (36) Schroder, D. K. In *Semiconductor Material and Device Characterization*; Wiley: New York, 1998; p 156.
- (37) Sporken, R.; Silien, C.; Malengreau, F.; Grigorov, K.; Caudano, R.; Sanchez, F. J.; Calleja, E.; Munoz, E.; Beaumont, B.; Gibart, P. *MRS Internet J. Nitride Semicond. Res.* **1997**, *2*, 23.
- (38) Goldberg, Yu. A.; Posse, E. A. *Semiconductors* **1998**, *32*, 181–183.